*Journal of Advanced Ceramics*
2022, **11**(10): 1583–1595
https://doi.org/10.1007/s40145-022-0631-1

ISSN 2226-4108
CN 10-1154/TQ

**Research Article**

# Facile fabrication of cordierite-based porous ceramics with magnetic properties

Hao LI[a], Cuiwei LI[a,*], Huaiming JIA[a], Guangjin CHEN[a], Siyuan LI[a], Kepi CHEN[b], Chang-An WANG[c], Liang QIAO[d]

[a]*Center of Materials Science and Engineering, School of Mechanical, Electronic and Control Engineering, Beijing Jiaotong University, Beijing 100044, China*
[b]*School of Energy, Power and Mechanical Engineering, North China Electric Power University, Beijing 102206, China*
[c]*State Key Laboratory of New Ceramics and Fine Processing, School of Materials Science and Engineering, Tsinghua University, Beijing 100084, China*
[d]*College of Materials Science and Engineering, Zhejiang University of Technology, Hangzhou 310014, China*

Received: April 28, 2022; Revised: May 21, 2022; Accepted: July 10, 2022


**Abstract:** In this paper, cordierite-based porous ceramics with magnetic properties have been firstly *in-situ* synthesized by using MgO, $Al_2O_3$, and $SiO_2$ powders as raw materials and $Fe_3O_4$ as a functional additive. Combining with the foam freeze casting method, near net size fabrication (total linear shrinkage < 2.86%) of the magnetic porous materials was realized by adjusting the amount of $Fe_3O_4$. The porosity, compressive strength, and saturation magnetization of the prepared materials were 83.9%–87.8%, 1.51–2.65 MPa, and 1.2–5.8 emu/g, respectively. The phase composition and microstructure evolutions during sintering were investigated briefly. The results showed that the synthesis temperature of cordierite was lowered about 100 ℃ due to the addition of $Fe_3O_4$. Except for the main phase-cordierite, Mg–Al–Fe spinel and α-$Fe_2O_3$ also existed in the final materials. The lattice parameters of the Mg–Al–Fe spinel and the amount of α-$Fe_2O_3$ changed obviously with the change in the sintering temperature and $Fe_3O_4$ amount, which mainly influenced the magnetic properties of the prepared materials. Thus, a facile fabrication method of the cordierite-based porous ceramics with the magnetic properties has been put forward in this paper.

**Keywords:** porous cordierite ceramics; phase composition; microstructure; magnetic property

## 1 Introduction

Due to their excellent properties, porous cordierite ceramics have been widely applied in many fields, such as gas filtration [1,2], catalyst carriers [3,4], air cleaners support [5], and so on. For those applications, high porosity is very important. However, the strength of the porous materials decreases rapidly as the porosity increases. Thus, it is significant to develop the materials with both high porosity and high strength. Recently, much research has been done to fabricate the materials with better properties [6–13]. In these studies,

* Corresponding author.
E-mail: cwli@bjtu.edu.cn

some results show that it is hard to obtain high-purity cordierite ceramics at low temperature through the solid-state reaction, and the most impurity phases usually have a negative performance impact [10–13].

To lower the synthesis or sintering temperature, additives have been widely used and proved to be effective [14–18]. For example, Li *et al*. [14] reported that the excess MgO increased the production of liquid and densification in the solid-state method. Guo *et al*. [15] studied the influence of $La_2O_3$ on the preparation and performance of the porous cordierite from rice husk, and found that the cordierite formation temperature decreased greatly with the addition of $La_2O_3$. Senthil Kumar *et al*. [16] found that the addition of $CeO_2$ benefited the synthesis of cordierite and the mechanical properties of the prepared materials. Moreover, Li *et al*. [18] prepared cordierite ceramics using kaolin, silicon dioxide, and magnesium oxide as raw materials, and studied the effects of $Fe_2O_3$ on the sintering behavior. They found that $Fe_2O_3$ promoted the sintering process and the content of the cordierite phase also increased. However, all these sintering additives could not give the material functionality, such as magnetic properties, electric or dielectric properties. The magnetic porous materials show broad prospects applied in supported catalysts [19], microwave absorbing [20], oil adsorption capacity [21], water treatment [22], biotechnology [23], and other fields [24,25] because of their large specific surface area and stable magnetic properties. For example, porous $Ni_xMg_yZn_{1-x-y}Fe_2O_4$ ferrites could be used in the area of magnetic carriers for the immobilized enzyme due to the strong adsorption properties, porous structure, and magnetic properties [25]. Introducing magnetism to the porous cordierite ceramics may improve their filtering or adsorption capacity to some certain extent due to the magnetic effect. Therefore, it is significant to find an additive that can not only reduce the synthesis temperature of cordierite, but also give the material magnetism.

To reduce the synthesis temperature of cordierite and give the material magnetism at the same time simply by introducing appropriate additives, $Fe_3O_4$ has come into our sight. Firstly, $Fe_3O_4$ has the same crystal structure as the intermediate phase spinel ($MgAl_2O_4$) when MgO, $Al_2O_3$, and $SiO_2$ were using as raw materials [10]. Thus, it may react with MgO and $Al_2O_3$ to form a Mg–Al–Fe–O solid solution with a spinel structure [26], which may be conducive to the synthesis of cordierite. Secondly, $Fe_3O_4$ is a typical ferrite with an inverse spinel crystal structure, which was usually used as a magnetic component in the magnetic porous materials [27–30]. Finally, the formed Mg–Al–Fe–O solid solution is one kind of ferrite which also can give the material magnetism.

In this work, a series of cordierite-based porous ceramics were *in-situ* synthesized by the foam gel-casting/foam freeze casting method using magnesia, alumina, and silica as raw materials and $Fe_3O_4$ as the functional additive. The effects of sintering temperature and $Fe_3O_4$ amount on the phase composition, microstructure, and properties have been researched. The purpose of this work is to investigate the effects of $Fe_3O_4$ on the phase composition evolution and magnetic properties of the cordierite-based porous ceramics, and finally to provide a strategy to endow and regulate the magnetic properties of the cordierite-based porous ceramics by introducing $Fe_3O_4$ as the functional additive.

## 2 Experimental

### 2. 1 Materials

High-purity ceramic powders of MgO (0.05 μm), $Al_2O_3$ (0.3 μm), and $SiO_2$ (10 μm) were used to synthesize the cordierite, and the $Fe_3O_4$ (0.5 μm) powders were used as the functional additive. The details of the raw materials and other reagents used in the experiment are shown in Table 1.

### 2. 2 Preparation

To study the effects of the sintering temperature, the porous samples were fabricated by the foam gel-casting method. Firstly, an initial solution containing AM, MBAM, ammonium polyacrylate, and deionized water was prepared. Then, the initial solution and the ceramic powders were ball-milled for 15 h to obtain a uniform slurry. The volume ratio of the ceramic powders to the deionized water was 1 : 3 in the slurry. After the addition of SDS and lauryl alcohol, the slurry was stirred (15 min) by a mechanical agitator rapidly. Then, TEMED and APS were added into the foamed slurry and stirred for another 5 min. Next, the obtained foamed slurry was poured into disposable paper molds with a diameter of 36 mm and gelled in 30 min to get a green body in the air. Lastly, the samples were dried by microwave equipment (BDMW-M-M-80, Henan Boda

**Table 1 Function, purity, and origin of raw materials and reagents used in the experiment**

| Material/reagent | Function | Purity (%) | Origin |
|---|---|---|---|
| Periclase | Raw material | 99.9 | Shanghai Macklin Biochemical Co., China |
| Corundum | Raw material | 99.9 | Beijing Boyu High-tech New Material Technology Co., China |
| Quartz | Raw material | 99.4 | Shanghai Fengchen Powder Material Co., China |
| Magnetite | Raw material | 97.0 | Sinopharm Chemical Reagent Co., China |
| Acrylamide (AM) | Monofunctional monomer | 99.5 | Sinopharm Chemical Reagent Co., China |
| N,N-methylene bis acrylamide (MBAM) | Crosslinker | 99.5 | Sinopharm Chemical Reagent Co., China |
| N,N,N′,N′-tetramethylethylenediamine (TEMED) | Accelerator | 99.5 | Sinopharm Chemical Reagent Co., China |
| Ammonium persulfate (APS) | Initiator | 99.7 | Xilong Chemical Industry Co., China |
| Ammonium polyacrylate | Dispersant | 99.5 | Shanghai Hengsheng Chemical Co., China |
| Sodium dodecyl sulfate (SDS) | Foam agent | 99.5 | Xilong Chemical Industry Co., China |
| Lauryl alcohol | Foam stabilizer | 99.5 | Sinopharm Chemical Reagent Co., China |
| Gelatin | Gel system | 95.0 | Sinopharm Chemical Reagent Co., China |
| Deionized water | Solvent | —— | —— |

Microwave Equipment Co., Ltd., China) and calcinated in the air at different temperatures with a heating rate of 1 ℃/min. Considering that the Fe ion could be dissolved into the cordierite crystal lattice to form iron cordierite [31], the mole ratio of MgO, $Al_2O_3$, $SiO_2$, and $Fe_3O_4$ was selected as 8 : 8 : 25 : 2. During the preparation, the dosage of each reagent is as follows: the mass ratio of the deionized water, AM, and MBAM was 100 : 10 : 1; the mass of APS was 15 wt% of AM; the mass of TEMED was 5 wt% of AM; the amount of ammonium polyacrylate was 6 wt% of ceramic powders; and the concentration of SDS was 2 g/L.

In order to adjust the magnetic properties on a large scale, the amount of $Fe_3O_4$ was designed from 8 to 25 wt%. Besides, the foam freeze-casting method [32] was selected to achieve near net size preparation of cordierite-based magnetic porous ceramics. The volume ratio of the ceramic powders to the deionized water was 1 : 4 in the slurry, the dosage of gelatin was 0.05 g/mL, and the concentration of SDS was 2 g/L. All the samples were sintered at 1340 ℃.

### 2. 3 Characterization

The dried green body and sintered specimens were ground to powders with a mortar. Then, the phase composition was investigated by X-ray diffraction (XRD, D8 ADVANCE A25, Bruker, Germany) with Cu Kα ($\lambda$ = 1.5418 Å) as the radiation, and the scanning speed was 6 (°)/min. Standard chromium powders were added to the sample powders in order to correct the instrument error, and then the XRD data were refined by Jade software. After that, the lattice parameters of the cordierite and Mg–Al–Fe spinel were calculated by Bragg equation ($n\cdot\lambda = 2d\cdot\sin\theta$). The microstructure, morphology, and elemental distribution of typical samples were examined by a scanning electron microscope (EVO 18, Carl Zeiss, Germany) equipped an energy dispersive spectroscope (EDS) operating at 15 kV. The heat and weight changes of the dried green body were evaluated by using a differential scanning calorimeter (DSC, 409 PC, Netzsch, Germany) in the air at a heating rate of 10 ℃/min up to 1400 ℃.

The prepared materials were ground into powders, and the magnetic properties of the related powders were measured by a vibration sample magnetometer (VSM, 8604, Lakeshore, USA) at room temperature. Open porosity and bulk density were tested by Archimedes method in distilled water. The compressive strength (the size of samples was $\phi$20 mm × 20 mm) was tested by a universal testing machine (WDW-100E, Jinan Times Assay Test Instrument Co. Ltd., China), and the loading rate was 0.5 mm/min. The drying linear shrinkage, sintering linear shrinkage, and total linear shrinkage were calculated by the inner diameter of the mold, dried green body, and sintered samples. A permeability tester (DSY Porous Ceramic Permeability Tester, Xiangtan Instrument and Instrument Co., Ltd., China) was used to measure the permeability of the distilled water, and the sample size was $\phi$20 mm × 10 mm. All these data were obtained from at least three samples.

## 3 Results and discussion

### 3. 1 Phase and microstructure evolution

#### *3.1.1 Thermal analysis*

The heat and weight changes of the dried green body during the sintering are shown in Fig. 1. From the differential thermal analysis (DTA) curve, two endothermic peaks (at 105 and 930 ℃) and three exothermic peaks (at 380, 1270, and 1310 ℃) were observed. Compared with the DTA curve without $Fe_3O_4$ as a sintering additive [10], the exothermic peak at 1369 ℃ relating to the synthesis of cordierite decreased obviously after the addition of $Fe_3O_4$, which indicated that the synthesis temperature of cordierite was lowered.

From the thermogravimetry (TG) curve in Fig. 1, four stages of the weight change were observed, which were different from the results without the addition of $Fe_3O_4$ in Ref. [10]. In that study, only three weight changes occurred below 1000 ℃ [10]. This result indicated that the addition of $Fe_3O_4$ also influenced the weight change during the sintering. Combined with the TG–DTA curves in Fig. 1 and our previous study [10,33], the initial weight loss (about 5 wt%) occurred from 50 to 200 ℃, which was caused by the removal of residual water and intramolecular dehydration of organics, corresponding to the above endothermic peak at 105 ℃; the second part of the weight loss (about 14.7 wt%) occurred between 200 and 600 ℃ was mainly due to the oxidative decomposition of organic residues, corresponding to the above exothermic peak at 380 ℃; and the third part of the weight loss (about 1.1 wt%) occurred at 800–1000 ℃, which was due to the elimination of the sulfur coming from APS and SDS. Above 1000 ℃, the fourth part of the weight loss occurred, which might be related to the addition of $Fe_3O_4$.

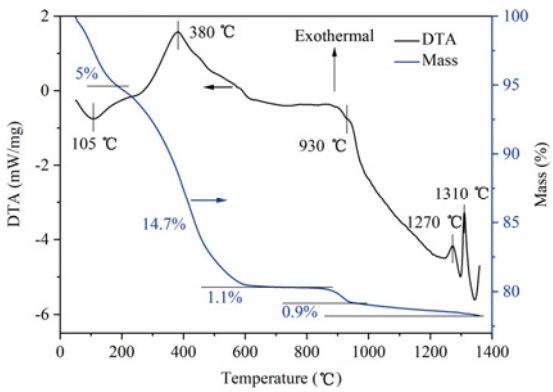


**Fig. 1** TG–DTA curves of dried green body.

#### *3.1.2 Phase composition of samples sintered at different temperatures*

To study the evolution of the phase composition during sintering, the dried green body was sintered at different temperatures. The typical images and XRD patterns of the dried green body and samples sintered at different temperatures are shown in Fig. 2. As shown in Fig. 2(a) (the diameter of the cylinders is about 30 mm), the sample color changed significantly from black to yellow, pale brown, brown, dark brown, and dark gray with increasing the sintering temperature. The color change of the samples sintered at different temperatures indicated that the phase composition changed obviously during the sintering, which was proved by the XRD patterns in Fig. 2(b).

From Fig. 2(b), the dried green body was composed of periclase, corundum, quartz, and magnetite which was basically consistent with the raw materials. Besides, the sintering temperature affected the phase composition greatly before 1320 ℃. The major phases of the samples sintered at 1240 ℃ were quartz, cristobalite, Mg–Al–Fe spinel (the crystal structure was consistent with that in JCPDS 01-089-8734), and sapphirine (JCPDS 00-044-1430), which was different from that of the dried green body. Especially, dark $Fe_3O_4$ changed into the Mg–Al–Fe spinel, leading the sample color change to yellow. When the sintering

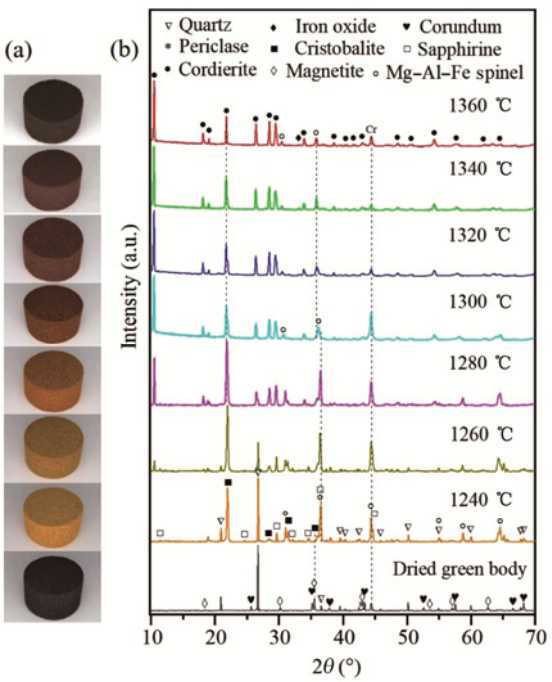


**Fig. 2** (a) Typical images and (b) XRD patterns of dried green body and samples sintered at different temperatures.

temperature increased to 1260 ℃, cristobalite became the main phase and the content of quartz decreased significantly. Meanwhile, the diffraction peaks of cordierite appeared. This phenomenon indicated that the cordierite was synthesized at 1260 ℃, which was much lower than that of the samples without $Fe_3O_4$ as the additive [10]. This result showed that the addition of $Fe_3O_4$ promoted the synthesis of cordierite effectively. According to the study of Wu *et al*. [34], $Fe^{3+}$ can substitute $Mg^{2+}$ or $Al^{3+}$ to form the solid solution in the $MgO–Al_2O_3–SiO_2$ system, which is beneficial for the synthesis of cordierite. In this study, the formation of the Mg–Al–Fe spinel had the same role. As sintering temperature increased further, the content of cordierite increased, and it became the first main phase in the samples sintered at 1300 ℃. Above 1300 ℃, the diffraction peak intensity of cordierite changed a little, showing that the cordierite had been mostly synthesized at this temperature. The synthesis temperature of cordierite was about 100 ℃ lower than that of the samples without $Fe_3O_4$ [10]. As sintering temperature increased to 1320 ℃, α-$Fe_2O_3$ with a rhombohedral crystal system (JCPDS 01-079-1741) appeared, and the diffraction peaks of the Mg–Al–Fe spinel shifted to the left. Over 1320 ℃, the diffraction peaks of the Mg–Al–Fe spinel and iron oxide were almost unchanged, while the diffraction peaks of cristobalite decreased gradually and finally disappeared at 1360 ℃.

According to the study on cordierite glass ceramics, irons could enter the cordierite lattice to form iron cordierite [31]. However, herein the diffraction peaks of the iron cordierite were not detected; the diffraction peaks of the cordierite sintered at different temperatures did not shift obviously and the lattice parameters of cordierite calculated by the Bragg equation were almost the same as those ($a$ = 16.9750 Å, $b$ = 9.7300 Å, $c$ = 9.3560 Å) of cordierite in Ref. [35]. In contrast, the positions of diffraction peaks of Mg–Al–Fe spinel varied obviously with the increase of sintering temperature. When sintering temperature increased from 1280 to 1320 ℃, the diffraction peaks of the Mg–Al–Fe spinel shifted to left gradually, which indicated the lattice parameters of the Mg–Al–Fe spinel increased. The average ionic radius of Fe ions was bigger than those of $Mg^{2+}$ and $Al^{3+}$. The large lattice parameter indicated that the proportion of Fe ion in the Mg–Al–Fe spinel was heightened at a high temperature. The high proportion of Fe ion in the Mg–Al–Fe spinel ferrite is favorable for its magnetism.

### *3.1.3 Typical microstructure of samples sintered at different temperatures*

Typical SEM images in Fig. 3 show the pore structure, skeletal microstructure of dried green body, and samples sintered at different temperatures. As shown in Fig. 3(a), micron spherical pores were obtained by this method, and the pore size was about 200 μm. After being sintered, many small window pores appeared on the large spherical pore wall. In addition, the number and size of the window pores expanded obviously as sintering temperature increased, which may be due to the uneven sintering shrinkage and the densification of the ceramic skeleton. It should be noted that the size of the large spherical pore is almost unchanged before and after the sintering. The SEM images at high magnification showed that the

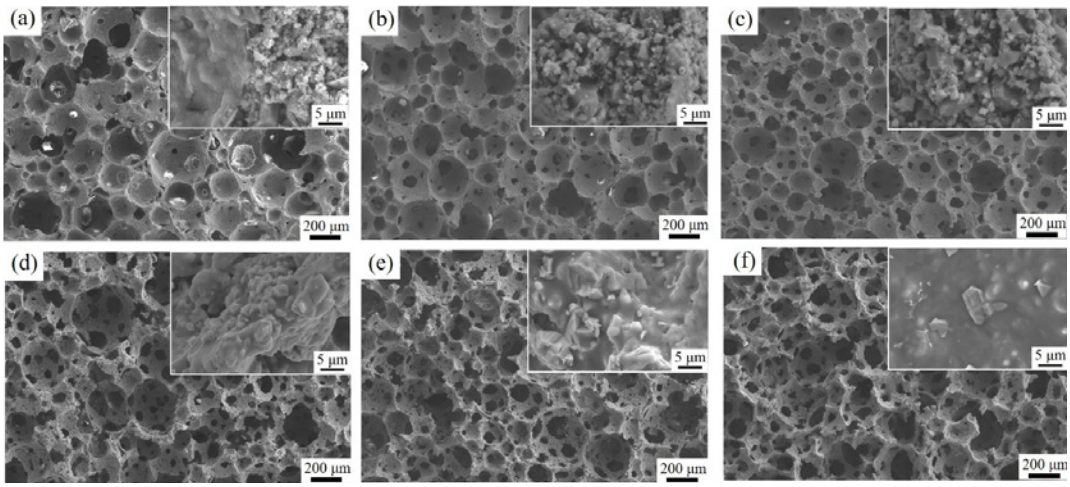


**Fig. 3** SEM images (pore microstructure and pore wall microstructure) of dried green body and magnetic porous ceramic at different sintering temperatures: (a) dried green body; (b) 1240 ℃; (c) 1280 ℃; (d) 1300 ℃; (e) 1340 ℃; and (f) 1360 ℃.

skeleton structure changed vastly during the sintering. Before the sintering, ceramic particles were connected by organics (polyacrylamide). As sintering temperature increased to 1240 ℃, sintering necks formed between the ceramic particles, and the skeleton became more densified. In addition, the liquid phase appeared at 1300 ℃ and its amount increased as the sintering temperature raised. The increase in the liquid phase was correlated to the change of cristobalite.

To determine the morphology of different phases, the element distribution of the typical samples was investigated by the EDS analysis, as shown in Fig. 4. According to the elemental mappings in Fig. 4(a), Si enrich particles were observed inside yellow circles. The size and shape of the Si enrich particles were consistent with the raw material of $SiO_2$. In addition, the distribution of Mg, Al, and Fe was basically the same, indicating the existence of the Mg–Al–Fe solid solution. From Fig. 2(b), cordierite also appeared at 1260 ℃, but the cordierite grains could not be distinguished from Fig. 4(a). This was mainly because the diffraction peak intensity of cordierite at 1260 ℃ in Fig. 2(b) was weak. As shown in Fig. 4(b), iron element is enriched in the small particles circled by the red line, and the distribution of Mg, Al, and Si was uniform in the matrix phase. Combining with Fig. 2(b), the small particles were the Mg–Al–Fe spinel or $Fe_2O_3$, and the matrix was mainly cordierite. Figure 4(b) also shows that the magnetic particles of the Mg–Al–Si spinel and $Fe_2O_3$ bonded tightly with the cordierite matrix.

### *3.1.4 Analysis of reaction mechanism*

To explore the influence of $Fe_3O_4$ on the *in-situ* synthesis of cordierite, the green body was calcined at 700, 800, 850, 900, and 930 ℃. The phase compositions of the samples were analyzed by the XRD and the results are shown in Fig. 5. Main phases of the samples calcined at 700 ℃ were MgO, $Al_2O_3$, $SiO_2$, $Fe_3O_4$, and α-$Fe_2O_3$. When the temperature increased, the diffraction peak intensity of α-$Fe_2O_3$ did not rise but fell down significantly. However, the diffraction peak intensity of $Fe_3O_4$ increased, and the diffraction peak intensity of $Fe_3O_4$ at 850 ℃ was almost similar to that of $Fe_3O_4$ in the dried green body. At this stage, the diffraction peak intensity of MgO, $Al_2O_3$, and $SiO_2$ barely changed.

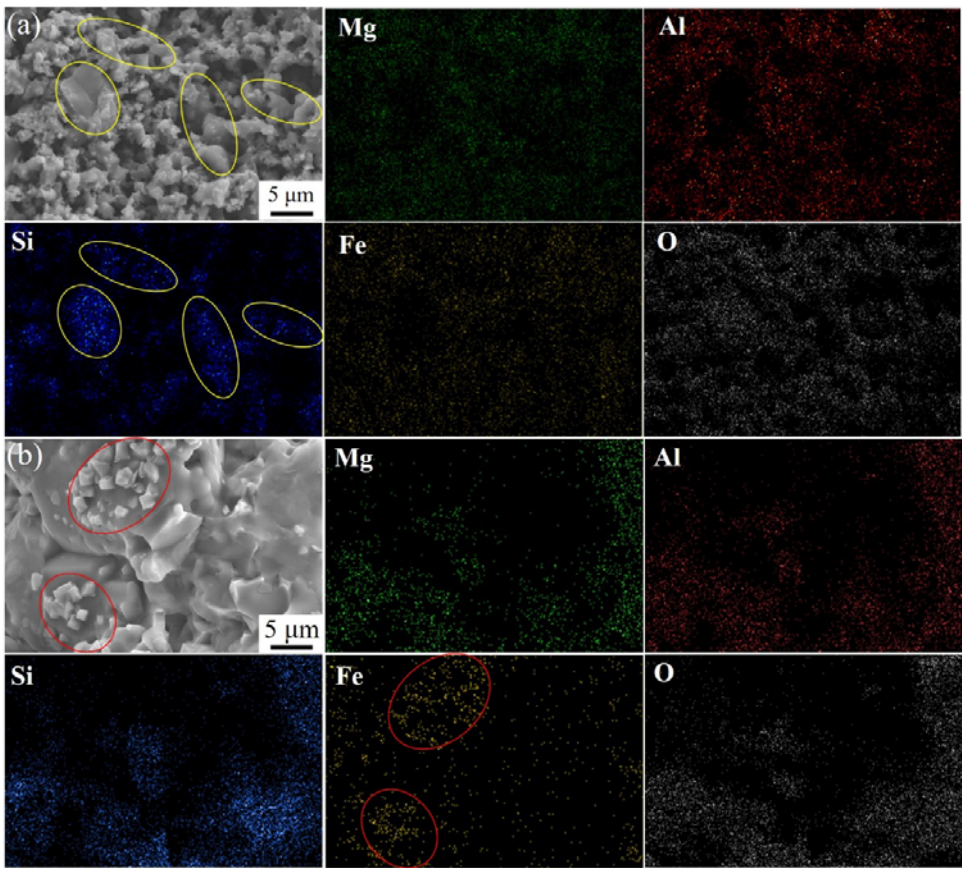


**Fig. 4** EDS mappings of samples sintered at different temperatures: (a) 1260 ℃ and (b) 1320 ℃.

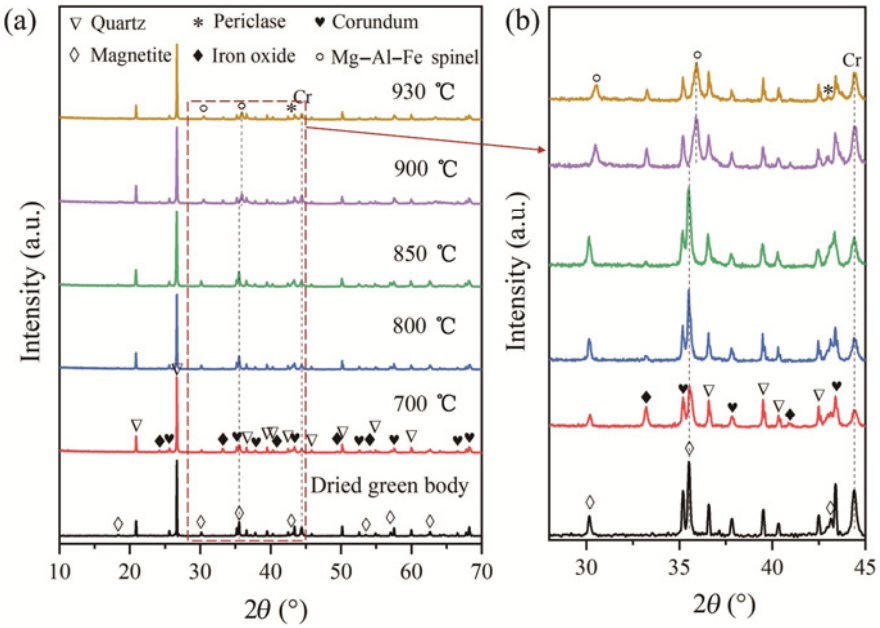


**Fig. 5** (a) XRD patterns of samples calcined at lower temperatures. (b) Local magnification of (a).

Based on the above results, the appearance of α-$Fe_2O_3$ at 700 ℃ indicated that $Fe_3O_4$ was oxidized when the temperature raised from room temperature to 700 ℃. However, when the temperature increased to 850 ℃, most of the α-$Fe_2O_3$ transformed to $Fe_3O_4$ again, which indicated that the mutual transformation of $Fe_3O_4$ and α-$Fe_2O_3$ occurred in this MgO–$Al_2O_3$–$SiO_2$–$Fe_3O_4$ system. Moreover, why such changes occurred is not clear and needs to be further studied. The above reactions could be shown in Eq. (1):

$$4Fe_3O_4 + O_2 \Leftrightarrow 6Fe_2O_3 \quad (1)$$

When the calcining temperature increased to 900 ℃, the diffraction peak intensity of MgO and $Al_2O_3$ decreased slightly, the diffraction peaks of $Fe_3O_4$ shifted to the right obviously and the diffraction peaks of $Fe_2O_3$ heightened. These results indicated that the Mg–Al–Fe spinel was synthesized from MgO, $Al_2O_3$, and $Fe_3O_4$ at this temperature corresponding to the endothermic peak of 930 ℃ from the DTA curve in Fig. 1. The possible reaction is shown as Eq. (2), in which the Mg–Al–Fe spinel is expressed as $Mg_xAl_yFe_zO_4$ because the atomic ratio of Mg, Al, and Fe in the Mg–Al–Fe spinel was unknown. The phase composition of the samples calcined at 930 ℃ was similar to that calcined at 900 ℃, indicating no new reaction happened.

$$Fe_3O_4 + Al_2O_3 + MgO \rightarrow Mg_xAl_yFe_zO_4\,(\text{spinel}) + Fe_2O_3 \quad (2)$$

From Fig. 2, as the sintering temperature increased to 1240 ℃, $Fe_2O_3$ disappeared, which indicated that all the Fe ions entered the crystal lattice of the Mg–Al–Fe spinel. In addition, the diffraction peaks of the Mg–Al–Fe spinel shifted to the right further, which means the proportion of Mg and Al in the samples sintered at 1240 ℃ was higher than that of the samples sintered at 930 ℃. Besides, according to the study on the reaction between magnesia chrome spinel and iron oxide in the solid phase by Cheng [36], the magnesia chrome spinel could react with the iron oxide to form the Mg–Cr–Fe solid solution. During the process of the solid solution reaction, a part of $Fe^{3+}$ changed into $Fe^{2+}$ and released ozone. Combined with Cheng's study, the possible reaction at this temperature is shown in Eq. (3), from which the weight loss above 1000 ℃ in Fig. 1 was related to the release of ozone.

$$Fe_2O_3 + Al_2O_3 + MgO + Mg_xAl_yFe_zO_4\,(\text{spinel}) \rightarrow Mg_{x1}Al_{y1}Fe_{z1}O_4\,(\text{spinel}) + O_3\uparrow \quad (3)$$

Meanwhile, the cristobalite appeared, and the sapphirine was also synthesized at this temperature. The crystallization phase of sapphirine ($Mg_3Al_9Si_2O_{20}$) was metastable [37]. The possible reactions are shown in Eqs. (4) and (5):

$$SiO_2\,(\text{quartz}) \rightarrow SiO_2\,(\text{cristobalite}) \quad (4)$$

$$Al_2O_3 + MgO + SiO_2 \rightarrow Mg_3Al_9Si_2O_{20} \quad (5)$$

When sintering temperature increased to 1260 ℃, most of the quartz transformed into the cristobalite. In addition, the distribution positions of Mg, Al, and Fe in Fig. 4(a) were basically the same, which proved that these particles were the Mg–Al–Fe spinel. After the appearance of cristobalite at 1240 ℃, the cordierite appeared at 1260 ℃. The possible reaction is presented

by Eq. (6):

$$Mg_{x1}Al_{y1}Fe_{z1}O_4\ (\text{spinel}) + SiO_2\ (\text{cristobalite}) \rightarrow Mg_2Al_4Si_5O_{18} + Mg_{x2}Al_{y2}Fe_{z2}O_4\ (\text{spinel}) \quad (6)$$

The diffraction peaks of quartz disappeared, and the diffraction intensity of cristobalite was the highest at 1280 ℃. It indicated that the quartz was completely transformed to the cristobalite, and then the Mg–Al–Fe spinel and cristobalite further reacted to form the cordierite. The possible reaction can be expressed in Eq. (7):

$$Mg_{x2}Al_{y2}Fe_{z2}O_4\ (\text{spinel}) + SiO_2\ (\text{cristobalite}) \rightarrow Mg_2Al_4Si_5O_{18} + Mg_{x3}Al_{y3}Fe_{z3}O_4\ (\text{spinel}) \quad (7)$$

After all quartz is converted into the cristobalite through the crystal transformation, large amounts of $Mg^{2+}$ and $Al^{3+}$ from the Mg–Al–Fe spinel reacted with the cristobalite to form the cordierite. Thus, a large amount of cordierite was generated, and the diffraction intensity of cordierite became the highest at 1300 ℃. Because part of $Mg^{2+}$ and $Al^{3+}$ from the Mg–Al–Fe spinel reacted to form the cordierite, the proportion of Fe ions in the Mg–Al–Fe spinel increased. The average ionic radius of Fe ions was bigger than those of $Mg^{2+}$ and $Al^{3+}$, so the diffraction peaks of the Mg–Al–Fe spinel shifted to the left. At the same time, the sapphirine reacted with the cristobalite to form the cordierite [37]. The possible reaction is presented in Eqs. (8) and (9), in which $x3$ and $y3$ on the left are greater than $x4$ and $y4$ on the right.

$$Mg_{x3}Al_{y3}Fe_{z3}O\ (\text{spinel}) + SiO_2\ (\text{cristobalite}) \rightarrow Mg_2Al_4Si_5O_{18} + Mg_{x4}Al_{y4}Fe_{z4}O_4\ (\text{spinel}) \quad (8)$$

$$Mg_3Al_9Si_2O_{20} + SiO_2\ (\text{cristobalite}) \rightarrow Mg_2Al_4Si_5O_{18} \quad (9)$$

As sintering temperature increased to 1320 ℃, the diffraction intensity of the Mg–Al–Fe spinel dropped slightly, and the diffraction peak of α-$Fe_2O_3$ appeared again (Fig. 2). From Fig. 4(b), the distribution position of Mg, Al, and Si tended to be uniform at 1320 ℃, which further proved that these particles are cordierite; and the proportion of Mg and Al was quite low in the Mg–Al–Fe spinel. The possible reaction is shown in Eq. (10):

$$Mg_{x4}Al_{y4}Fe_{z4}O_4 + SiO_2 \rightarrow Mg_2Al_4Si_5O_{18} + Mg_{x5}Al_{y5}Fe_{z5}O_4 + Fe_2O_3 \quad (10)$$

The phase changed a little when the sintering temperature increased from 1320 to 1340 ℃. The diffraction peaks of cristobalite disappeared at 1360 ℃. In addition, it can be seen from the microstructure at low magnification in Fig. 3(f) that the small pores on the spherical pore wall continued to grow with the increase of temperature. The growth of the small pores on the pore wall may be mainly related to the appearance of the liquid phase in the later stage of the sintering. Besides, the microstructure at high magnification also showed the existence of the liquid phases at 1360 ℃.

## 3. 2 Properties of samples sintered at different temperatures

### *3.2.1 Porosity and compressive strength*

The sintering linear shrinkage, open porosity, and compressive strength of the samples sintered at different temperatures are shown in Fig. 6. The large sintering shrinkage (over 14%) at 1360 ℃ caused cracking and failure of the samples. Thus, the properties of those samples were not tested.

As sintering temperature increased from 1240 to 1320 ℃, the sintering shrinkage firstly remained unchanged, then decreased, and finally increased. However, the variation range of the sintering shrinkage was narrow, only changing from 2.15% to 3.29%. In addition, the sintering shrinkage of these samples was generally small, because the volume expansion derived from the phase evolution could partly compensate for the sintering shrinkage [38]. The cordierite has a relatively lower theoretical density than the main raw materials, which can lead to volume expansion during the sintering. Combined with Fig. 2(b), a large amount of cordierite was synthesized at 1300 ℃. Thus, the sintering shrinkage did not increase but decreased. The increase of the sintering shrinkage at 1340 ℃ was mainly due to the appearance of silicon-rich liquid phase.

As shown in Fig. 6, the open porosity was 83.9%–88.3%, and the compressive strength was 1.46–2.65 MPa. Meanwhile, the trend of compressive strength was opposite to the change of open porosity. Compared

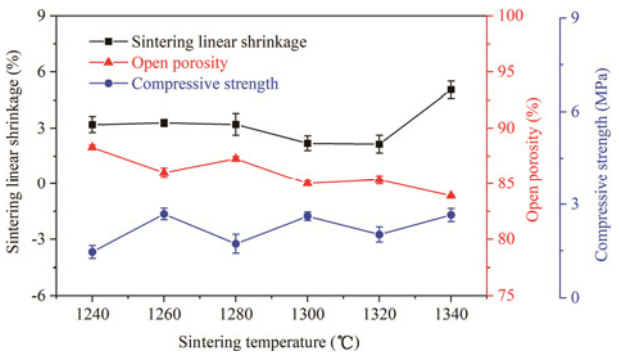


**Fig. 6** Sintering shrinkage, open porosity, and compressive strength of samples sintered at different temperatures.

with the materials prepared by other methods, the results (Fig. 6) showed that the materials prepared here presented both higher porosity and compressive strength. The porous cordierite prepared by the *in-situ* solid-state reactions [39] showed a porosity of 33.16% and a compressive strength of 72.64 MPa. The porous cordierite with the porosity of 86.9%–89.5% and the compressive strength of 0.22–0.44 MPa was obtained by thermo-foaming [40]. Herein, the high porosity of the samples was due to the high foam volume during the preparation and the small shrinkage during the sintering. The high strength was caused by the high equability of the spherical pores and the small sintering deformation [41]. The compressive strength of the samples with an open porosity of ~83% in this paper was slightly smaller than that of the samples without additive [10], which was mainly because there were a large number of window pores on the spherical pore wall (Fig. 3).

### *3.2.2 Magnetic properties*

The samples sintered at or above 1300 ℃ could be easily attracted by magnets and dragged off the ground, which are shown in Figs. 7(a) and 7(b). Considering the magnetic properties and phase composition, the hysteresis loops of the two typical samples sintered at 1300 and 1340 ℃ were measured by vibrating the sample magnetometer, as shown in Fig. 7(c). When the sintering temperatures were 1300 and 1340 ℃, the values of $M_s$ were calculated to be 3.7 and 4.8 emu/g, the values of $M_r$ were 0.2 and 0.3 emu/g, and the $H_c$ were 20 and 30 Oe, respectively. The results indicated that the composite ceramics were easy to be magnetized by an external magnetic field and easy to demagnetize due to their low coercive force. The hysteresis loops showed that the samples were soft magnetic materials with low magnetizing power and hysteresis loss. The variation in the $M_s$ value of the samples sintered at 1300 or 1340 ℃ was mainly due to the phase evolution. Firstly, the diffraction peaks of the Mg–Al–Fe spinel became sharper at 1340 ℃ in Fig. 2(b), suggesting the improvement of crystallinity. Secondly, the lattice constant of the Mg–Al–Fe spinel rose from 8.29 to 8.33 Å when the temperature increased from 1300 to 1340 ℃, indicating that the proportion of iron ions in the Mg–Al–Fe spinel increased at 1340 ℃. Finally, α-$Fe_2O_3$ occurred in the samples sintered at 1340 ℃, which also had magnetism [42].

## 3.3 Effect of $Fe_3O_4$ amount on cordierite-based porous ceramics

### *3.3.1 Phase composition*

The XRD patterns of the samples with different $Fe_3O_4$ amounts are shown in Fig. 8. All the samples were mainly composed of cordierite, Mg–Al–Fe spinel (the crystal structure was consistent with that in JCPDS 01-089-8734), and iron oxide with a rhombohedral crystal system (JCPDS 01-079-1741). With the increase of $Fe_3O_4$ content, the diffraction peaks of cordierite are basically unchanged, but the amount of the Mg–Al–Fe spinel and iron oxide increased obviously. Meanwhile, the diffraction peaks of the Mg–Al–Fe spinel shifted to the left when the $Fe_3O_4$ amount changed from 8 to 20 wt%, and the lattice constant of the Mg–Al–Fe spinel was calculated to be 8.20, 8.29, 8.32, 8.33, and 8.32 Å

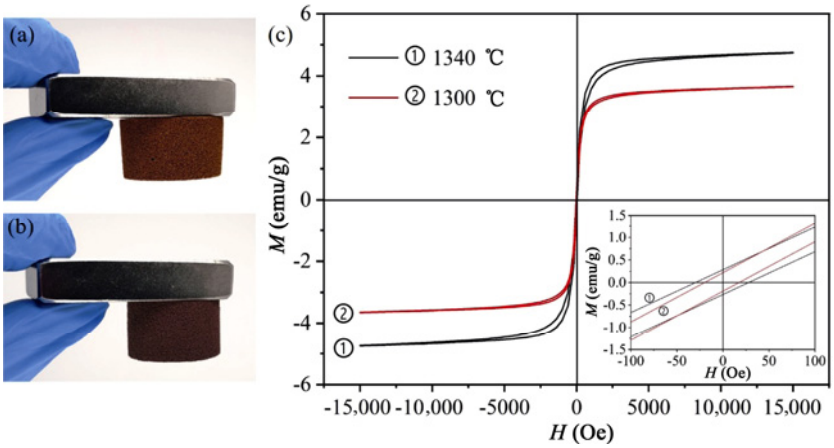


**Fig. 7** (a, b) Photographs showing attraction of magnet to samples sintered at 1300 and 1340 ℃, respectively. (c) Hysteresis loops of samples sintered at 1300 and 1340 ℃.

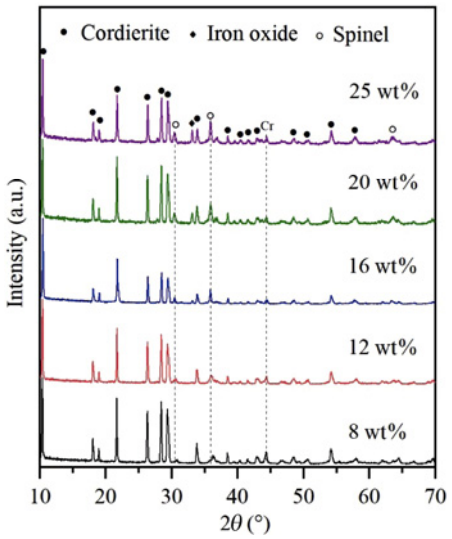


**Fig. 8** XRD patterns of samples with different $Fe_3O_4$ amounts.

as the $Fe_3O_4$ amount was 8, 12, 16, 20, and 25 wt%, respectively.

### *3.3.2 Microstructure*

The SEM images of the cordierite-based porous ceramics with different $Fe_3O_4$ amounts are shown in Fig. 9. From the microstructure at low magnification, the pore size of the spherical pores in different samples changed slightly. However, the number of window pores on the spherical pore wall increased with the rise of $Fe_3O_4$ amount. As seen from the microstructure at high magnification in Fig. 9, the grains grew obviously with the increase of $Fe_3O_4$ content. From Fig. 9(j), microcracks appeared in the samples with 25 wt% $Fe_3O_4$, which would affect the strength of the materials.

### *3.3.3 Properties*

The linear shrinkage of the samples with different $Fe_3O_4$ amounts is shown in Fig. 10. With the increase of $Fe_3O_4$ amount, the drying shrinkage changed slightly only fluctuating between 1.20% and 1.45%, but the sintering shrinkage increased obviously from −0.94% to 6.99%. The results indicated that the amount of $Fe_3O_4$ had little effect on the drying shrinkage, but influenced the sintering linear shrinkage prominently. It was found that the samples expanded during the sintering when the amount of $Fe_3O_4$ was 8 wt%. In addition, when the amount of $Fe_3O_4$ rose from 8 to 16 wt%, the total shrinkage was between 0.50% and 2.86%, lower than 3% [43], which indicated that the near net shape fabrication of the cordierite-based porous ceramics with magnetism was realized.

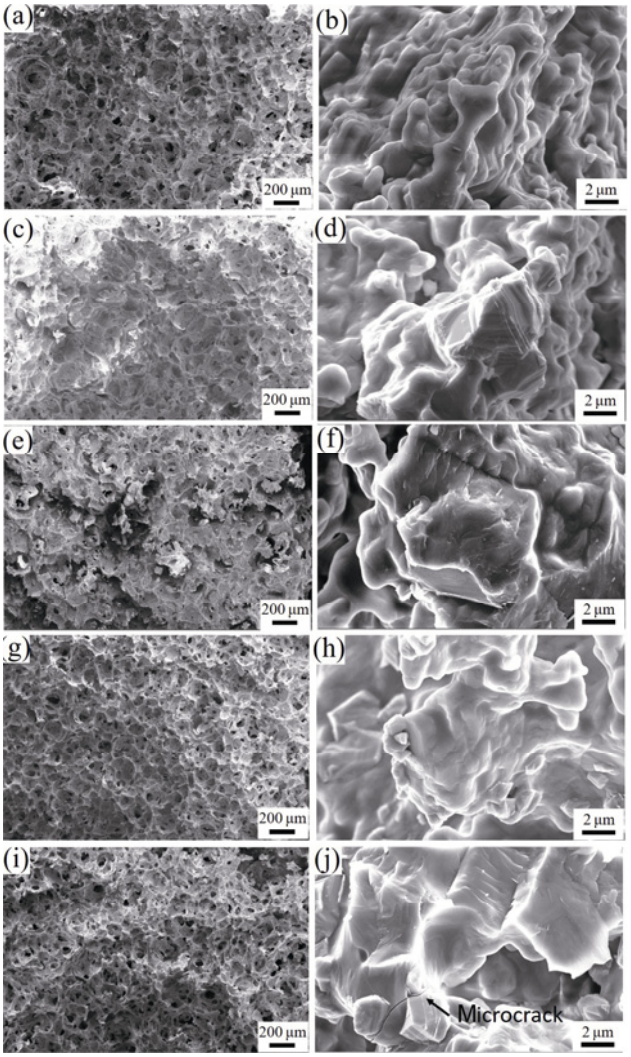


**Fig. 9** SEM images of cordierite-based magnetic porous ceramics with different $Fe_3O_4$ amounts of: (a, b) 8 wt%; (c, d) 12 wt%; (e, f) 16 wt%; (g, h) 20 wt%; and (i, j) 25 wt%.

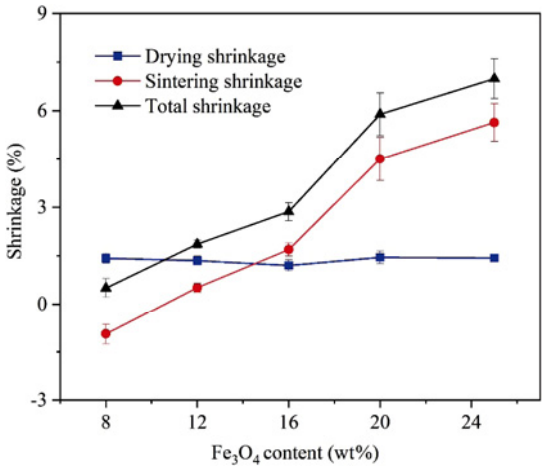


**Fig. 10** Linear shrinkage of the samples with different $Fe_3O_4$ amounts.

The open porosity, bulk density, compressive strength, and permeability coefficient of the samples with different $Fe_3O_4$ amounts were tested, and the results are shown in Fig. 11. With the increase of $Fe_3O_4$ amount, the open porosity of the samples decreased from 87.8% to 86.0%, and the bulk density increased from 0.31 to 0.40 g/cm$^3$. The variation of porosity is mainly derived from the change of sintering shrinkage. As shown in Fig. 11, when the $Fe_3O_4$ amount increased from 8 to 25 wt%, the compressive strength increased first from 1.51 to 1.92 MPa, and then decreased to 1.36 MPa. As shown in Fig. 9(j), the microcracks generally existed in the samples when the $Fe_3O_4$ content was 25 wt%, resulting in the lowest compressive strength (1.36 MPa) of the samples. Even so, its compressive strength was higher than that (1.22 MPa) of the samples with the same porosity [10]. As the $Fe_3O_4$ amount increased from 8 to 25 wt%, the permeability coefficient changed from $2.2\times10^{-11}$ to $7.4\times10^{-11}$ m$^2$ roughly, showing an increasing trend. The changing trend of permeability was opposite to that of porosity. Combined with the pore structure in Fig. 9, both the number and the size of the window pores became larger, which help fluid pass through the pores. Thus, the permeability enlarged obviously under the condition of little change in the porosity. Moreover, the permeability of the materials with 25 wt% $Fe_3O_4$ is twice that ($3.65\times10^{-11}$ m$^2$) of the samples without $Fe_3O_4$ as the additive [44].

The hysteresis loops of the samples with different $Fe_3O_4$ contents are presented in Fig. 12, and the values of $M_s$, $M_r$, and $H_c$ were calculated and summarized in Table 2. As the $Fe_3O_4$ content increased from 8 to 25 wt%, the $M_s$ increased from 1.2 to 5.8 emu/g, the $H_c$ changed from 80 to 145 Oe, and the $M_r$ was 0.3–1.4 emu/g. The change of $M_s$ was mainly caused by the variety of the Mg–Al–Fe spinel and α-$Fe_2O_3$ contents in the samples. As shown in Fig. 8, the amount of the Mg–Al–Fe spinel and $Fe_2O_3$ rose with the increase of the $Fe_3O_4$ content. In addition, the lattice constant of the Mg–Al–Fe spinel firstly increased and then remained stable with the increased of the $Fe_3O_4$ content. The increase of iron proportion in the Mg–Al–Fe spinel will also increase the $M_s$ of the materials. Furthermore, the $H_c$ and $M_r$ of the samples were low, which indicated that the prepared porous ceramic was soft magnetic material.

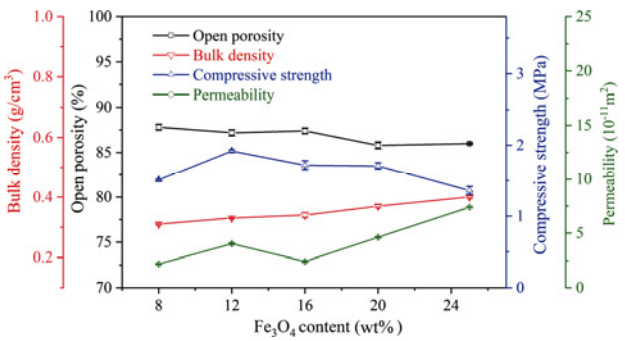


**Fig. 11** Open porosity, bulk density, compressive strength, and permeability of samples with different $Fe_3O_4$ amounts.

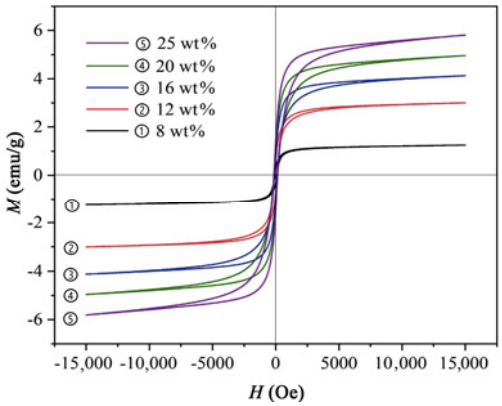


**Fig. 12** Hysteresis loops of samples with different $Fe_3O_4$ amounts.

**Table 2 Magnetic properties of samples with different $Fe_3O_4$ amounts**

| $Fe_3O_4$ amount (wt%) | $M_s$ (emu/g) | $H_c$ (Oe) | $M_r$ (emu/g) |
|---|---|---|---|
| 8 | 1.2 | 80 | 0.3 |
| 12 | 3.0 | 110 | 0.7 |
| 16 | 4.1 | 110 | 0.9 |
| 20 | 5.0 | 135 | 1.2 |
| 25 | 5.8 | 145 | 1.4 |

On the whole, the addition of $Fe_3O_4$ not only promoted the synthesis of cordierite, but also lowered the sintering temperature of the prepared materials. Especially, it endowed magnetic properties to the prepared cordierite-based porous ceramics. Thus, through this method, the cordierite-based porous ceramics with the magnetic properties can be easily prepared, and the magnetic properties can be manipulated by adjusting the sintering temperature and $Fe_3O_4$ amount. Meanwhile, the prepared samples possess high porosity, high strength, and high permeability.

## 4 Conclusions

In this paper, cordierite-based porous ceramics with

magnetic properties, high porosity, and high strength have been easily prepared by combining the *in-situ* synthesis with the foam gel-casting method, wherein MgO, $Al_2O_3$, and $SiO_2$ are used as raw materials and $Fe_3O_4$ as the functional additive.

As the sintering temperature increased from 1240 to 1340 ℃, the main phases changed vastly, and the final crystalline phases were the cordierite, Mg–Al–Fe spinel, and α-$Fe_2O_3$. The open porosity of the samples sintered at different temperatures was between 83.9% and 88.3%, and the compressive strength was 1.46–2.68 MPa. When the sintering temperature was 1300 and 1340 ℃, the values of $M_s$ were 3.7 and 4.8 emu/g, respectively. The Mg–Al–Fe spinel and iron oxide were the main origin of magnetism.

The magnetic properties of the cordierite-based porous ceramics could also be manipulated by adjusting the $Fe_3O_4$ amount. When the weight ratio of $Fe_3O_4$ was 8–25 wt%, the $M_s$ was 1.2–5.8 emu/g, the open porosity was 86.0%–87.8%, the bulk density was 0.31–0.40 g/cm$^3$, the compressive strength was 1.36–1.92 MPa, and the permeability coefficient was $2.2\times10^{-11}$–$7.4\times10^{-11}$ m$^2$. When the weight ratio of $Fe_3O_4$ was 8–16 wt%, the near net shape fabrication of the cordierite-based magnetic porous ceramics was realized with a total sintering shrinkage of 0.50%–2.86%.

This work provides a strategy to endow and regulate the magnetic properties of the cordierite-based porous ceramics through the incorporation of $Fe_3O_4$ as the functional additive.

## Acknowledgements

This work was supported by the Fundamental Research Funds for the Central Universities (Grant Nos. 2020YJS148 and 2022JBZY025), State Key Laboratory of New Ceramics and Fine Processing Tsinghua University (Grant No. KFZD201902), Beijing Natural Science Foundation (Grant No. 2182059), and the Beijing Government Funds for the Constructive Project of Central Universities.

## Declaration of competing interest

The authors have no competing interests to declare that are relevant to the content of this article.

## References

[1] Senguttuvan TD, Kalsi HS, Sharda SK, *et al*. Sintering behavior of alumina rich cordierite porous ceramics. *Mater Chem Phys* 2001, **67**: 146–150.

[2] Du YF, Wen BL, Shu RL, *et al*. Potassium titanate whiskers on the walls of cordierite honeycomb ceramics for soot catalytic combustion. *Ceram Int* 2021, **47**: 34828–34835.

[3] Mohamed Shamshuddin SZ, Sundar MS, Thimmaraju N, *et al*. Synthesis, characterization and catalytic activity studies on cordierite honeycomb coated with $ZrO_2$ based solid super acids. *Comptes Rendus Chimie* 2012, **15**: 799–807.

[4] Zhou TQ, Li LD, Cheng J, *et al*. Preparation of binary washcoat deposited on cordierite substrate for catalytic applications. *Ceram Int* 2010, **36**: 529–534.

[5] Yao Y, Ochiai T, Ishiguro H, *et al*. Antibacterial performance of a novel photocatalytic-coated cordierite foam for use in air cleaners. *Appl Catal B* 2011, **106**: 592–599.

[6] Liu J, Dong YC, Dong XF, *et al*. Feasible recycling of industrial waste coal fly ash for preparation of anorthite-cordierite based porous ceramic membrane supports with addition of dolomite. *J Eur Ceram Soc* 2016, **36**: 1059–1071.

[7] Zhang XZ, Fang DR, Lin B, *et al*. Asymmetric porous cordierite hollow fiber membrane for microfiltration. *J Alloys Compd* 2009, **487**: 631–638.

[8] Parlak TT, Demirkiran AS. Zeolite usage as source of silica to produce cordierite in MgO–$Al_2O_3$–$SiO_2$ system. *J Adv Ceram* 2018, **7**: 370–379.

[9] Wang LL, Ma BY, Ren XM, *et al*. Phase-engineering strategy of $ZrO_2$ for enhancing the mechanical properties of porous cordierite ceramics. *Mater Today Commun* 2022, **30**: 103032.

[10] Li H, Li CW, Wu LH. Porous cordierite ceramics prepared by foam-gelcasting technique: Phase evolution and properties. *J Alloys Compd* 2019, **791**: 690–699.

[11] Vakalova TV, Pogrebenkov VM, Revva IB, *et al*. Effect of fluorine-containing additive on the synthesis and sintering of compositions from natural raw materials in the "cordierite–mullite" system. *Ceram Int* 2019, **45**: 9695–9703.

[12] Wang WB, Shi ZM, Wang XG, *et al*. The phase transformation and thermal expansion properties of cordierite ceramics prepared using drift sands to replace pure quartz. *Ceram Int* 2016, **42**: 4477–4485.

[13] Ogiwara T, Noda Y, Shoji K, *et al*. Solid state synthesis and its characterization of high density cordierite ceramics using fine oxide powders. *J Ceram Soc Jpn* 2010, **118**: 246–249.

[14] Li Y, Cheng XD, Zhang RF, *et al*. Effect of excess MgO on the properties of cordierite ceramic sintered by solid-state method. *Int J Appl Ceram Technol* 2015, **12**: 443–450.

[15] Guo W, Lu HB, Feng CX. Influence of $La_2O_3$ on preparation and performance of porous cordierite from rice husk. *J Rare Earths* 2010, **28**: 614–617.

[16] Senthil Kumar M, Elaya Perumal A, Vijayaram TR. Synthesis, characterization and sintering behavior influencing

mechanical, thermal and physical properties of pure cordierite and cordierite-ceria. *J Adv Ceram* 2015, **4**: 22–30.

[17] Ren XM, Ma BY, Zhang YR, *et al*. Effects of sintering temperature and $V_2O_5$ additive on the properties of SiC–$Al_2O_3$ ceramic foams. *J Alloys Compd* 2018, **732**: 716–724.

[18] Li Y, Zhao HZ. Effect of $Fe_2O_3$ addition on sintering behavior of cordierite ceramic obtained by solid-state sintering method. *J Aust Ceram Soc* 2019, **55**: 567–574.

[19] Lu AH, Schmidt W, Matoussevitch N, *et al*. Nanoengineering of a magnetically separable hydrogenation catalyst. *Angew Chem Int Ed Engl* 2004, **43**: 4303–4306.

[20] Wang LX, Guan YK, Qiu X, *et al*. Efficient ferrite/Co/porous carbon microwave absorbing material based on ferrite@metal-organic framework. *Chem Eng J* 2017, **326**: 945–955.

[21] Yang SD, Chen L, Mu L, *et al*. Magnetic graphene foam for efficient adsorption of oil and organic solvents. *J Colloid Interface Sci* 2014, **430**: 337–344.

[22] Ling L, Zhang WX. Enrichment and encapsulation of uranium with iron nanoparticle. *J Am Chem Soc* 2015, **137**: 2788–2791.

[23] Borlido L, Azevedo AM, Roque ACA, *et al*. Magnetic separations in biotechnology. *Biotechnol Adv* 2013, **31**: 1374–1385.

[24] Peretyat'ko PI, Kulikov LA, Melikhov IV, *et al*. Magnetic porous composite material: Synthesis and properties. *Tech Phys Lett* 2015, **41**: 974–976.

[25] Qi X, Zhou X, Shu D, *et al*. Effect of porous structure on the magnetic properties of $Ni_xMg_yZn_{1-x-y}Fe_2O_4$ magnetic materials. *Chin Phys Lett* 2011, **28**: 107502.

[26] Wang JN, Novaro O, Li CL. Mössbauer spectroscopy and X-ray diffraction studies of Mg–Al–Fe–O mixed spinel sulphur transfer catalysts. *J Mater Sci* 1998, **33**: 3671–3676.

[27] Lee CC, Yoshikawa N, Taniguchi S. Microwave-induced substitutional-combustion reaction of $Fe_3O_4$/Al ceramic matrix porous composite. *J Mater Sci* 2011, **46**: 7004–7011.

[28] Sandeep Kumar TK, Viswanathan NN, Ahmed HM, *et al*. Estimation of sintering kinetics of magnetite pellet using optical dilatometer. *Metall Mater Trans B* 2016, **47**: 309–319.

[29] Huang YM, Zhai BG, Ma QL, *et al*. Magnetic properties of ferrous ferric oxide confined in porous silicon. *Mater Sci Forum* 2010, **663–665**: 1142–1145.

[30] Tan P, Jiang Y, Liu XQ, *et al*. Magnetically responsive porous materials for efficient adsorption and desorption processes. *Chin J Chem Eng* 2019, **27**: 1324–1338.

[31] Wang S. Effects of Fe on crystallization and properties of a new high infrared radiance glass-ceramics. *Environ Sci Technol* 2010, **44**: 4816–4820.

[32] Li H, Li JW, Li CW, *et al*. Near net shape fabrication of porous cordierite by combination of foam gel-casting and freeze-drying. *Int J Appl Ceram Technol* 2021, **18**: 2121–2131.

[33] Li CW, Han Y, Wu LH, *et al*. Synthesis and growth of anorthite crystal during *in situ* preparation of porous anorthite ceramics by foam-gelcasting. *Int J Appl Ceram Technol* 2017, **14**: 957–962.

[34] Wu WQ, Ruan YZ, Yu Y. Influence of $Fe_2O_3$ impurity on the crystalline structure of cordierite synthesized from waste aluminum slag. *Chinese J Struc Chem* 2005**, 24**: 483–487.

[35] Koepke J, Schulz H. Single crystal structure investigations under high-pressure of the mineral cordierite with an improved high-pressure cell. *Phys Chem Miner* 1986, **13**: 165–173.

[36] Cheng JJ. Reaction of Mg–Cr spinel with iron oxide in solid phase. *J Chin Ceram Soc* 1965, **4**: 30–42. (in Chinese)

[37] De Vekey RC, Majumdar AJ. Nucleation and crystallization studies of some glasses in the CaO–MgO–$Al_2O_3$–$SiO_2$ system. *Mineral Mag* 1970, **37**: 771–779.

[38] Li H, Li CW, Wu LH, *et al*. Near net size sintering of porous cordierite ceramics with excellent properties. *J Alloys Compd* 2020, **826**: 154121.

[39] Wang SX, Wang H, Chen ZW, *et al*. Fabrication and characterization of porous cordierite ceramics prepared from fly ash and natural minerals. *Ceram Int* 2019, **45**: 18306–18314.

[40] Li X, Li YB, Xiang RF, *et al*. Effect of dispersion viscosity on microstructure of cordierite foam prepared by thermo-foaming. *Ceram Int* 2019, **45**: 24487–24492.

[41] Gibson LJ, Ashby MF. *Cellular Solids*. Cambridge: Cambridge University Press, 1997.

[42] Cao M, Liu T, Gao S, *et al*. Single-crystal dendritic micro-pines of magnetic α-$Fe_2O_3$: Large-scale synthesis, formation mechanism, and properties. *Angew Chem Int Ed Engl* 2005, **44**: 4197–4201.

[43] Krause T, Molotnikov A, Carlesso M, *et al*. Mechanical properties of topologically interlocked structures with elements produced by freeze gelation of ceramic slurries. *Adv Eng Mater* 2012, **14**: 335–341.

[44] Li H, Li CW, Wu LH, *et al*. *In-situ* synthesis and properties of porous cordierite ceramics with adjustable pore structure. *Ceram Int* 2020, **46**: 14808–14815.